Contrasting Cu Roles Lead to High Ranged Thermoelectric Performance of PbS

HPSTAR
1281-2021

Yongxin Qin, Tao Hong, Bingchao Qin, Dongyang Wang, Wenke He, Xiang Gao, Yu Xiao,* and Li-Dong Zhao*

To obtain high-performance PbS-based thermoelectric materials, this study introduces Cu with different contrasting roles in *p*-type PbS, which can effectively decrease the lattice thermal conductivity and simultaneously optimize the electrical transport properties. Experimental results illustrate that Cu substitutions and Cu interstitials can improve carrier mobility through lowering effective mass (m^*) and carrier concentration (n_H) in a low temperature range (300–450 K), and further optimize temperature-dependent n_H in a high temperature range (450–823 K). Both decreased m^* and n_H shift the peak power factor to low temperature range, leading to an ultrahigh power factor $\approx 23\ \mu W\ cm^{-1}\ K^{-2}$ at 423 K for $Pb_{0.99}Cu_{0.01}S$-0.01Cu. Additionally, the special dynamic-doping behaviors of Cu can continuously promote n_H to approach the temperature-dependent relationship of $(n_{H,\ opt}) \approx (m^*T)^{1.5}$, which brings about an eminent average power factor (PF_{ave}) $\approx 18\ \mu W\ cm^{-1}\ K^{-2}$ among 300–823 K in $Pb_{0.99}Cu_{0.01}S$-0.01Cu. Furthermore, the microstructure characterizations unclose that the atomic and nanoscale Cu-containing defects can effectively intensify the phonon scattering and suppress the lattice thermal conductivity. Consequently, both high ZT (≈ 0.2 at 300 K) and peak ZT (≈ 1.2 at 773 K) result in a record-high average ZT (ZT_{ave}) of ≈ 0.79 at 300–823 K for $Pb_{0.99}Cu_{0.01}S$-0.01Cu.

1. Introduction

Thermoelectric technology, as a clean and renewable energy conversion technology, has attracted wide attention in the fields of physics, materials science, energy fields, and chemistry since the waste heat can be directly transformed to electricity power.[1–4] However, limited by the low conversion efficiency and cost performance of thermoelectric technology, large-scale practical application is difficult to achieve. The thermoelectric

conversion efficiency is evaluated by the dimensionless figure of merit, *ZT*. *ZT* can be expressed as $(PF/\kappa_{tot})/T$, $PF = S^2\sigma$, and $\kappa_{tot} = \kappa_{ele} + \kappa_{lat}$, where σ, S, PF, κ_{tot}, κ_{lat}, κ_{ele}, and T are electrical conductivity, Seebeck coefficient, power factor, total thermal conductivity, lattice thermal conductivity, electronic thermal conductivity and absolute temperature in Kelvin, respectively.[5–10] High *ZT* value needs both low total thermal conductivity (κ_{tot}) and good electrical transport properties (*PF*) simultaneously. However, it is challengeable to achieve high *ZT* value owing to the competing relationship between charge and phonon transports in thermoelectric materials.

To improve *ZT* value, researchers are seeking diverse strategies of enhancing carrier transport properties by tuning carrier concentration (n_H),[11–15] revising the band structure[16–19] or reducing lattice thermal conductivity (κ_{lat}) through designing all scale hierarchical defects, such as mesoscale grain boundaries,[20–23] nanoprecipitates,[24–29] dislocations,[30–33] and interstitials.[34–36] To date, the defects engineering to reduce κ_{lat} has been well developed and successfully proven to be effective.[37–41] However, the designed defects in thermoelectric materials not only strengthen phonon scattering, they can also cause extra carrier scattering, then resulting in deteriorated electrical transport properties. Therefore, the approaches of elaborately optimizing the carrier-related effective mass (m^*) and n_H to maintain high electrical transport properties are crucial. Low m^* can contribute to enhanced carrier mobility (μ_H) based on the relationship of $\mu \propto 1/m^*$,[42] thus in high electrical transport properties as well elucidated in PbTe-SnSe,[43] PbTe-MnTe,[44] and PbS-Sn[45] systems. Meanwhile, n_H optimization can effectively balance *S* and σ, finally producing a high average power factor (PF_{ave}) when the temperature-dependent n_H approaches an optimal relationship of $(n_{H,\ opt}) \approx (m^*T)^{1.5}$ (where $n_{H,\ opt}$, m^* and *T* are the optimal carrier concentration, effective mass and absolute temperature in Kelvin, respectively),[46] as well established in PbTe-In/Ga[47–49] and PbTe/Se-Cu systems.[35,50,51] Apparently, m^* and n_H are two key parameters to determine the electrical transport properties and final thermoelectric performance.[52–55]

This work focuses on the earth-abundant and low-cost PbS-based thermoelectric material, which is known as a promising

Dr. Y. Qin, Dr. T. Hong, Dr. B. Qin, Dr. D. Wang, Dr. W. He, Dr. Y. Xiao, Prof. L.-D. Zhao
School of Materials Science and Engineering
Beihang University
Beijing 100191, China
E-mail: xiao_yu@buaa.edu.cn; zhaolidong@buaa.edu.cn
Prof. X. Gao
Center for High Pressure Science
and Technology Advanced Research (HPSTAR)
Beijing 100094, China

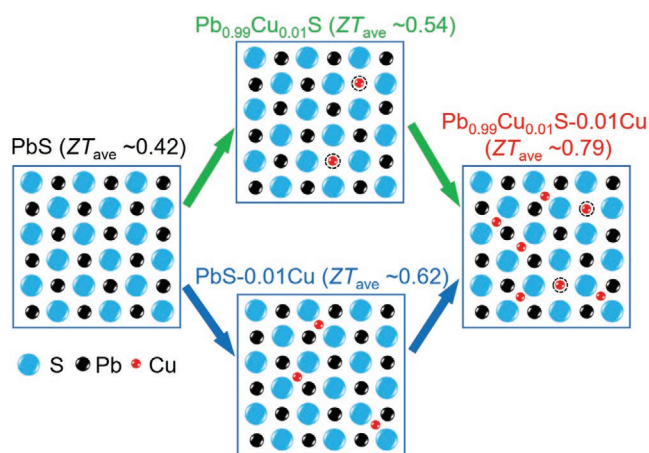**Figure 1.** Roadmaps toward ultrahigh ZT_{ave} achieved in p-type $Pb_{0.99}Cu_{0.01}S$-0.01Cu via compositing Cu in the forms of substitutions ($Pb_{0.99}Cu_{0.01}S$) and interstitials (PbS-0.01Cu). the carrier concentration for all the samples have been optimized, which was fixed with the fraction of 2% Li.

candidate of PbTe. However, compared with PbTe, PbS exhibits comparably lower PF and higher κ_{lat}.[56,57] Based on these strongly coupled thermoelectric relationships, Cu is introduced in p-type PbS to synergistically manipulate the carrier and phonon transport properties. Herein, we systematically investigate the different Cu roles in p-type PbS, including Cu substitutions, Cu interstitials and both of them. **Figure 1** shows that contrasting Cu roles in p-type PbS can evidently boost the average ZT (ZT_{ave}) from ≈0.42 for Cu-free PbS to ≈0.54 and ≈0.62 at 300–823 K, respectively, and further enhancement of ZT_{ave} ≈ 0.79 can be achieved with both Cu substitutions and Cu interstitials in p-type PbS. Hall experimental results unclose that Cu substitutions and Cu interstitials in p-type PbS can reduce m^* at low temperature range (300–450 K) and also exhibit a dynamic doping in high temperature range (450–823 K), and then a high PF_{ave} of ≈18 μW cm^{-1} K^{-2} at 300–823 K is achieved in $Pb_{0.99}Cu_{0.01}S$-0.01Cu. Meanwhile, microstructure observations reveal that Cu can form atomic and nanoscale defects that can largely suppress κ_{lat} from ≈0.9 W m^{-1} K^{-1} at 823 K in PbS to ≈0.6 W m^{-1} K^{-1} at 823 K in $Pb_{0.99}Cu_{0.01}S$-0.01Cu.

2. Results and Discussion

The designing strategy for enhancing the thermoelectric performance of p-type PbS can be described below as several successive reasonable steps. First, p-type PbS was obtained using Li element as an acceptor doping. Second, based on the optimized thermoelectric transport properties (Figures S1–S3, Supporting Information), 2% Li doping fraction was selected (since all the samples have been doped with the fixed fraction of 2% Li, Li was excluded when named the samples in the case of clear expressing the idea of this work), different Cu forms (Cu substitutions $Pb_{0.99}Cu_{0.01}S$ and Cu interstitials PbS-0.01Cu) are separately imported in p-type PbS matrix to investigate their outstanding and contrasting roles in enhancing thermoelectric performance. Third, both Cu substitutions

and Cu interstitials are concurrently introduced in p-type PbS matrix ($Pb_{0.99}Cu_{0.01}S$-0.01Cu) that synergistically optimize the carrier and phonon transport properties. Thermoelectric properties with p-type PbS, PbS-0.01Cu, $Pb_{0.99}Cu_{0.01}S$ and $Pb_{0.99}Cu_{0.01}S$-Cu0.01 samples are systematically investigated through comparing Hall experiments and microstructure observations to reveal its origin of enhanced thermoelectric performance.

2.1. Comparisons of Electrical Transport Properties for PbS, PbS-0.01Cu, $Pb_{0.99}Cu_{0.01}S$, and $Pb_{0.99}Cu_{0.01}S$-0.01Cu Samples

The thermoelectric transport properties for Cu substitutions ($Pb_{1-z}Cu_zS$), Cu interstitials (PbS-yCu), and both Cu substitutions and Cu interstitials ($Pb_{1-h}Cu_hS$-hCu) are shown in Figures S4–S12 in the Supporting Information. To clearly investigate the contrasting roles of Cu, 1% was selected for comparison, which is shown in **Figure 2**. In Figure 2a) compared with σ of PbS, the σ of PbS-0.01Cu, $Pb_{0.99}Cu_{0.01}S$ and $Pb_{0.99}Cu_{0.01}S$-0.01Cu samples obviously decrease from ≈1280, ≈2110, and ≈1670 S cm^{-1} at 300 K to ≈102, ≈157, and ≈140 S cm^{-1} at high temperature. Correspondingly, compared with S of PbS, the S of PbS-0.01Cu, $Pb_{0.99}Cu_{0.01}S$ and $Pb_{0.99}Cu_{0.01}S$-0.01Cu samples increases in the entire temperature range, Figure 2b which results from the decreased n_H. Notably, the temperature-dependent σ and S for PbS-0.01Cu, $Pb_{0.99}Cu_{0.01}S$ and $Pb_{0.99}Cu_{0.01}S$-0.01Cu samples exhibit a slight turning point at around 573 K, which is mainly caused by the continuously increasing n_H at high temperature range in Figure 2b. The dynamic doping behaviour of Cu atom is generally observed in other lead-based chalcogenides, such as PbSe[35] and PbTe.[58]

It can be seen that introducing different Cu forms (Cu substitutions and Cu interstitials) has remarkable different results in PbS. To clarify Cu existence and its effects on n_H, in Figure S13 in the Supporting Information, the control samples of PbS with extra 1% Cu (PbS-0.01Cu without Li doping) and PbS with doping 1% Cu ($Pb_{0.99}Cu_{0.01}S$ without Li doping) are synthesized for comparison. Interestingly, PbS-0.01Cu shows n-type transport and $Pb_{0.99}Cu_{0.01}S$ shows p-type transport. Taking in account the variations in S and n_H, it illustrates that Cu exists in the form of interstitials in PbS-0.01Cu, while Cu acts a dopant in $Pb_{0.99}Cu_{0.01}S$. As a result, in this work, even though after doping Li for all the samples, it could be concluded that Cu atoms are interstitials in p-type PbS-0.01Cu and Cu atoms are substitutions in p-type $Pb_{0.99}Cu_{0.01}S$. Furthermore, the change of n_H with temperature in Figure 2c shows that Cu exists in PbS as a kind of dynamic dopant. The low n_H is benefit for electrical transport properties in the low temperature range, and the n_H presents a strongly temperature-dependent relationship in the high temperature range, which is following with the relationship of $(n_{H,opt}) \approx (m^*T)^{1.5}$.[46] After dynamic optimizing n_H, the μ_H at 300 K is noticeably improved from ≈115 cm^2 V^{-1} s^{-1} for PbS to ≈425, ≈332, and ≈476 cm^2 V^{-1} s^{-1} for PbS-0.01Cu, $Pb_{0.99}Cu_{0.01}S$ and $Pb_{0.99}Cu_{0.01}S$-0.01Cu, respectively, which might mainly arise from the reduced m^* and/or n_H after introducing Cu, in Figure 2d will be discussed later. The temperature-dependent μ_H in PbS-0.01Cu, $Pb_{0.99}Cu_{0.01}S$ and $Pb_{0.99}Cu_{0.01}S$-0.01Cu well follows the acoustic phonon dominated scattering relationship
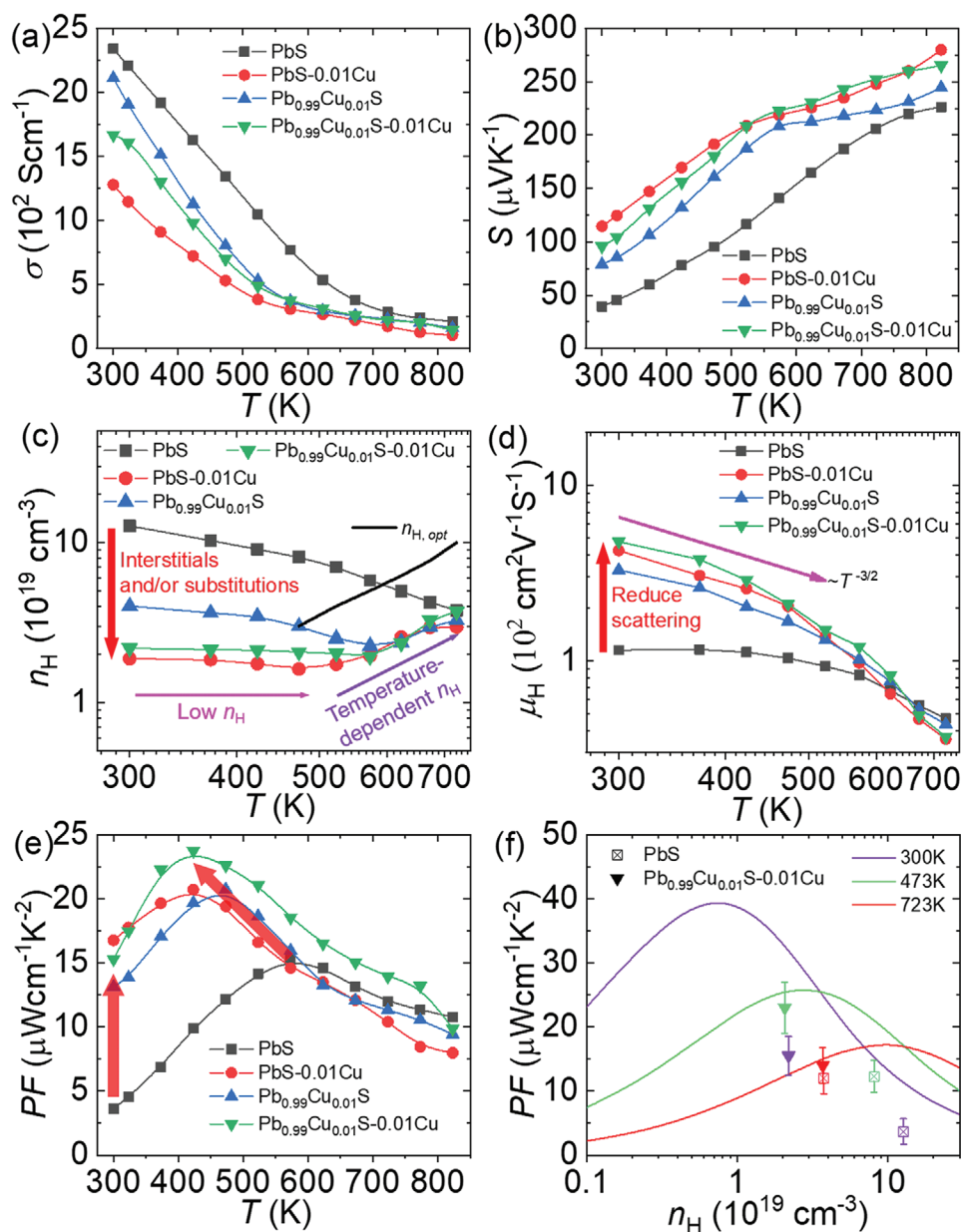
Figure 2. Comparisons of electrical transport properties for PbS, PbS-0.01Cu, $Pb_{0.99}Cu_{0.01}S$ and $Pb_{0.99}Cu_{0.01}S$-0.01Cu samples: a) σ; b) S; c) n_H; d) μ_H; e) PF; and f) calculated PF of p-type PbS and $Pb_{0.99}Cu_{0.01}S$-0.01Cu. All the samples are doped with 2% Li.

of $u_H \approx T^{-3/2}$ [59] at 300–573 K and then obviously deviates the line at high temperature range due to the intensified carrier–carrier scattering with increased u_H.

Consequently, Figure 2e shows that the PF for PbS-0.01Cu, $Pb_{0.99}Cu_{0.01}S$ and $Pb_{0.99}Cu_{0.01}S$-0.01Cu can be significantly enhanced in the entire temperature range, which is caused by the multiple positive effects of optimizing temperature-dependent n_H in the relative high temperature range and reducing n_H in the low temperature range. The room-temperature PF for PbS is enhanced from ≈3.6 to ≈15 μW cm⁻¹ K⁻² for $Pb_{0.99}Cu_{0.01}S$-0.01Cu, with an improvement of ≈320%, and the peak PF is increased from ≈15 μW cm⁻¹ K⁻² at 573 K for PbS to ≈23 μW cm⁻¹ K⁻² at

423 K for $Pb_{0.99}Cu_{0.01}S$-0.01Cu. The PF for $Pb_{0.99}Cu_{0.01}S$-0.01Cu is obviously improved in the entire temperature range, especially higher PF is achieved at low temperature compared with that of PbS. As a result, higher room-temperature PF and peak PF are obtained in $Pb_{0.99}Cu_{0.01}S$-0.01Cu. Figure 2f displays the calculated PF as a function of carrier concentrations at different temperatures. The experimental PF of $Pb_{0.99}Cu_{0.01}S$-0.01Cu well matches the calculated PF at high temperature range, much higher PF can be expected through further optimizing thermoelectric parameters. To clarify which thermoelectric parameters are effective to achieve PF enhancement, the theoretical electrical transport properties are calculated with Kane band model.[42,60]

2.2. Theoretically Predicted Power Factor with Optimal Relationship between m^* and n_H

According to these coupled relationships between thermoelectric parameters, m^* and n_H are two important parameters to determine the electrical transport properties. The theoretically predicted PF can achieve its maximum value in the entire working temperature range if the m^* and n_H meet an optimal relationship $(n_{H,opt}) \approx (m^*T)^{1.5}$.[46] Within Kane band model, the m^* plays a key role in tuning $n_{H, opt}$. Herein, high thermoelectric performance was achieved through controlling m^*. The electrical transport properties of PbS with both Cu substitutions and Cu interstitials ($Pb_{0.99}Cu_{0.01}S$-0.01Cu) are calculated through single Kane band model and the n_H can be writing as[46,47]

$$n_H = R_H^{-1} \frac{N_v (2m_b^* k_B T)^{3/2}}{2\pi^2 \hbar^3} {}^0F_0^{3/2} \tag{1}$$

where R_H, m_b^*, N_v, T, $\hbar$, k_B, and are the Hall factor, the effective band mass ($m^* = (N_v)^{2/3} m_b^*$), the band degeneracy ($N_v = 4$ for p-type PbS),[61] absolute temperature in Kelvin, the reduced Planck's constant and the Boltzmann constant, respectively. The Hall factor can be writing as[46,47]

$$R_H = \frac{3K(K+2)}{(2K+1)^2} \frac{{}^0F_{-4}^{1/2}\,{}^0F_0^{3/2}}{{}^0F_{-2}^1} \tag{2}$$

where K, ${}^nF_k^m$ are the band anisotropy factor ($K = 3.6$ for PbS)[47] and a similar form to the Fermi integral

$${}^nF_k^m = \int_0^\infty \left(-\frac{\partial f}{\partial \varepsilon}\right) \varepsilon^n \left(\varepsilon + \alpha\varepsilon^2\right)^m \left[(1+2\alpha\varepsilon)^2 + 2\right]^{k/2} d\varepsilon \tag{3}$$

where α, ε and E_g are mutually reduced band gap ($\alpha = k_B T/E_g$), reduced energy of the electronic state, and the band gap ($E_g/eV = 0.29 + 0.0004T$ for p-type PbS),[62] respectively.

PF and ZT are written as[46]

$$PF = \frac{2N_v \hbar k_B^2 C_1}{\pi E_{def}^2} \frac{1}{m_1^*} \left(\frac{{}^1F_{-2}^1}{{}^0F_{-2}^1} - \xi\right)^2 {}^0F_{-2}^1 \tag{4}$$

$$ZT = \frac{\left(\dfrac{{}^1F_{-2}^1}{{}^0F_{-2}^1} - \xi\right)^2}{\left[\dfrac{{}^2F_{-2}^1}{{}^0F_{-2}^1} - \left(\dfrac{{}^1F_{-2}^1}{{}^0F_{-2}^1}\right)^2\right] + \dfrac{{}^0F_{-2}^1}{3B^1F_{-2}^1}} \tag{5}$$

$$B = \frac{2Tk_B^2 \hbar C_1 N_v}{3\pi m_1^* E_{def}^2 \kappa_{lat}} \tag{6}$$

$$m_1^* = \frac{3m^*}{N_v^{2/3}\left(2K^{1/3} + K^{-2/3}\right)} \tag{7}$$

where m_1^*, C_1 and E_{def} present the inertial mass, the average longitudinal elastic modulus ($C_1 = 1.11 \times 10^{11}$ Pa for PbS),[60] and the deformation potential coefficient (calculated $E_{def} = 24$ eV for p-type PbS).

Figure 3a shows PF in different n_H as a function of m^*, and μ_H is negatively correlated with m^* according to the relationship of $\mu \propto 1/m^*$, therefore, higher PF needs the lower m^*. In this work, different Cu forms, including Cu substitutions and Cu interstitials, are imported into p-type PbS matrix, and the calculated m^* in $Pb_{0.99}Cu_{0.01}S$-0.01Cu evidently decreases at 300–450 K compared with PbS sample in Figure 3b which can largely improve PF in the low temperature range. In lead chalcogenides, the band gap and the band effective mass are positively correlated.[45] As shown in Figure S14 in the Supporting Information, the results of measured band gap illustrate that introducing Cu substitutions and/or Cu interstitials can decrease m^* because of the decreasing band gap. To verify whether n_H has reached the optimized level, Figure 3c displays the calculated PF for $Pb_{0.99}Cu_{0.01}S$-0.01Cu at different temperatures, the black line represents the $n_{H, opt}$. Theoretical results indicate that the maximum PF at different temperature require an increasing n_H, therefore, a dynamic n_H could contribute higher PF_{ave}, as well as elucidated in Figure 3d Therefore, the experimental PF values in the entire temperature range (PF_{ave}) are obtained in $Pb_{0.99}Cu_{0.01}S$-0.01Cu, which predominantly result from the lower m^* and temperature-dependent dynamic optimized n_H through introducing both Cu substitutions and Cu) interstitials in $Pb_{0.99}Cu_{0.01}S$-0.01Cu.

2.3. Lattice Thermal Conductivity and Microstructure Observations

Apart from significantly enhance PF_{ave}, both the low n_H at low temperature and the temperature-dependent n_H at high temperature and can also noticeably reduce the κ_{ele} (Figure S15, Supporting Information), which contributes to a significant low κ_{tot}, as shown in **Figure 4**a. The C_p is calculated by Debye model, which is compared with the experimental data, and more details about it can be found in Figure S16 in the Supporting Information. Figure 4b shows that κ_{lat} of PbS is also reduced after introducing Cu, it can be seen that the room-temperature κ_{lat} for PbS is ≈2.5 W m^{-1} K^{-1}, while it can be further depressed to as low as ≈1.4 W m^{-1} K^{-1} for $Pb_{0.99}Cu_{0.01}S$-0.01Cu, a decrease of ≈43%. The minimum κ_{lat} ($\kappa_{lat, min}$) for $Pb_{0.99}Cu_{0.01}S$-0.01Cu at 823 K is ≈0.6 W m^{-1} K^{-1}, which is much smaller than that of PbS (≈0.9 W m^{-1} K^{-1} at 823 K). According to the BvK-Pei model,[63] the $\kappa_{lat, min}$ of PbS is estimated, and the calculated $\kappa_{lat, min}$ of PbS is ≈0.2 W m^{-1} K^{-1}, which is smaller than that of $Pb_{0.99}Cu_{0.01}S$-0.01Cu. Therefore, there is still a large room to further reduce the lattice thermal conductivity in PbS. Both Cu substitutions and Cu interstitials for $Pb_{0.99}Cu_{0.01}S$-0.01Cu lead a much lower κ_{lat} than that of PbS-0.01Cu and $Pb_{0.99}Cu_{0.01}S$.

To disclose the low κ_{lat} in $Pb_{0.99}Cu_{0.01}S$-0.01Cu, Scanning Electron Microscopy (SEM), Energy-Dispersive Spectroscopy (EDS), Transmission Electron Microscopy (TEM), Scanning Transmission Electron Microscopy (STEM), Annual Bright Field (ABF), and Annular Dark-Field (ADF) are conducted to analysis the microstructures of $Pb_{0.99}Cu_{0.01}S$-0.01Cu. SEM images and corresponding EDS element mappings illustrate that the nanoscale precipitates are widely distributed in PbS matrix and the precipitates are rich with Cu atoms, Figure S17 in the Supporting Information. Meanwhile, nanoprecipitates
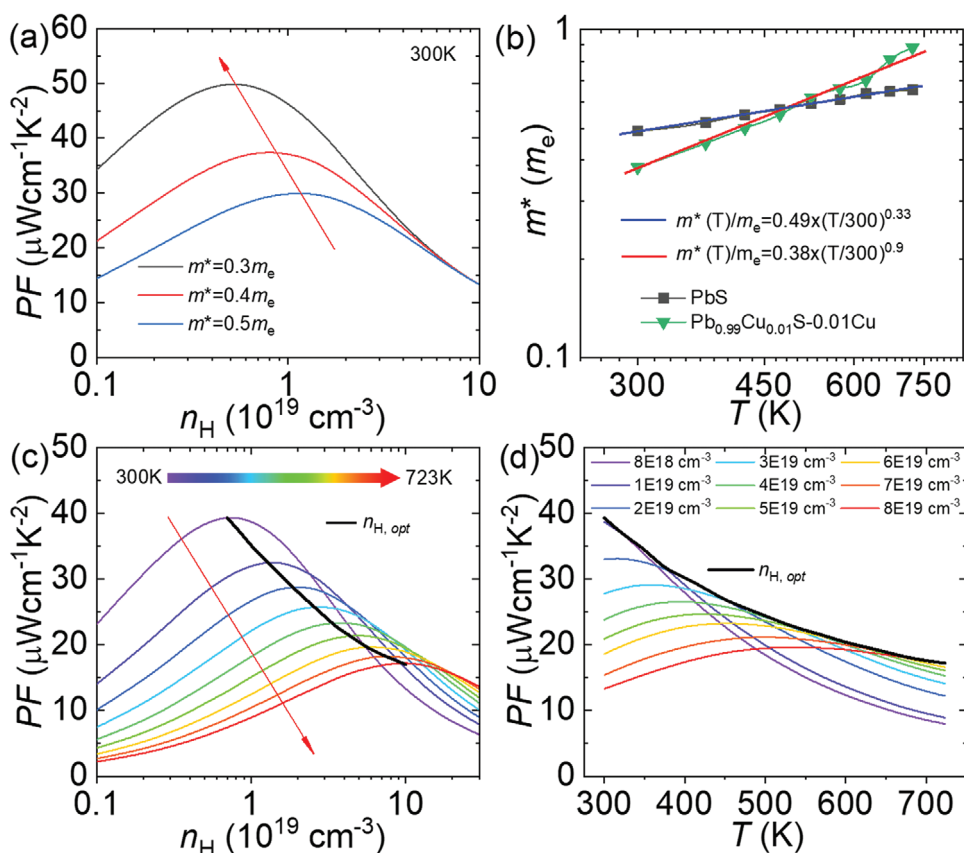
Figure 3. a) PF in different n_H as a function of m^* ($m^* = 0.3\ m_e$, $0.4\ m_e$, $0.5\ m_e$); b) temperature-dependent m^* for 2% Li doped PbS and $Pb_{0.99}Cu_{0.01}S$-0.01Cu; c) PF in different n_H as a function of temperature; and d) PF in different temperature as a function of n_H.

are significantly observed from ADF images and corresponding EDS element mappings including Pb, S and Cu (Figure S18, Supporting Information). In order to clarify the existence of nanoprecipitates in the PbS matrix, as shown in **Figure 5**a the TEM image for $Pb_{0.99}Cu_{0.01}S$-0.01Cu is obtained from electron-diffraction along [111] (Figure 5b and STEM ABF image for $Pb_{0.99}Cu_{0.01}S$-0.01Cu is clearly observed the interstitial Cu atoms in PbS (Figure S19, Supporting Information). Figure 5c

displays a great number of nano-scale precipitates with ≈20 nm to ≈100 nm. Figure 5e,f are two different morphologies of nanoprecipitates, where Figure 5e is obtained from electron-diffraction along [111] (Figure 5g Figure 5h displays the boundary (which is plotted by the white dotted line) between the matrix and the nanoprecipitate. We found that the nanoprecipitates in Figure 5h are semi-coherent, which may be caused by Cu interstitials, Cu substitutions, and Cu clusters. Traditionally, the
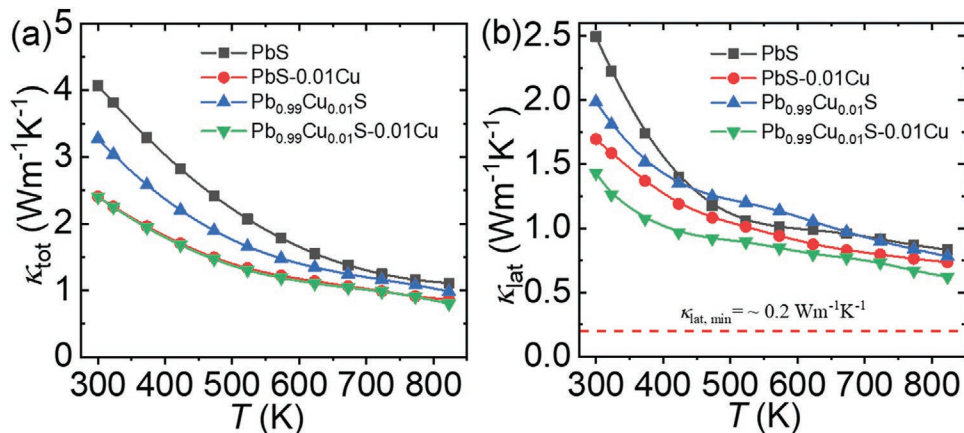

Figure 4. Thermal conductivity for PbS, PbS-0.01Cu, $Pb_{0.99}Cu_{0.01}S$ and $Pb_{0.99}Cu_{0.01}S$-0.01Cu: a) κ_{tot}; b) κ_{lat}. All the samples are doped with 2% Li.
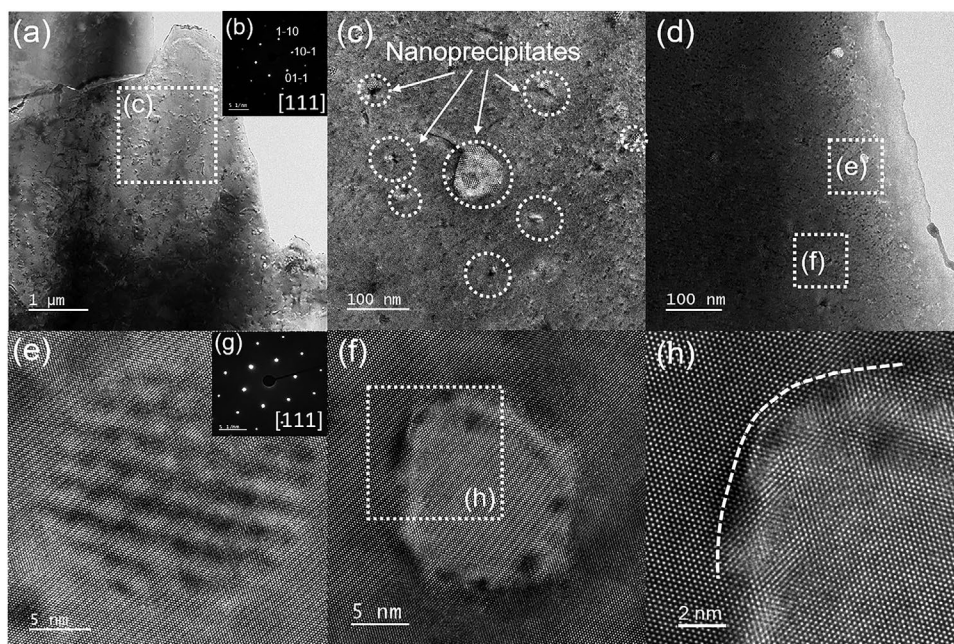
Figure 5. Nanoprecipitates in $Pb_{0.99}Cu_{0.01}S$-0.01Cu with 2% Li doping: a) low magnification TEM image and is obtained from b) electron-diffraction along [111]; c) considerable nanoprecipitates and d) middle magnification TEM image; e,f) Two different morphologies of nanoprecipitates; g) electron-diffraction along [111]; h) the boundary between the matrix and the nanoprecipitate is plotted by the white dotted line.

semi-coherent nanoprecipitates can significantly affect phonon scattering but slightly depress the carrier transport.[64] Therefore, it can be concluded that the semi-coherent nanoprecipitates in $Pb_{0.99}Cu_{0.01}S$-0.01Cu can scatter significantly phonons, while marginally affect the carrier transport on the basis of the calculated phonon and carrier mean free path in PbTe/Se.[65]

Figure 6a displays the room-temperature μ_H as a function of n_H for different p-type PbS thermoelectric materials including PbS, PbS-yCu, $Pb_{1-z}Cu_zS$, $Pb_{1-h}Cu_hS$-hCu, PbS-Na,[25] PbS-Ag,[66] and PbS- (SrS/CaS,[25] ZnS/CdS[67]). The μ_H and n_H are two competing parameters, introducing Cu substitutions and Cu interstitials can further optimizes μ_H and n_H, making them approach the theoretically μ_H line. Compared with reported p-type PbS samples,[25,66,67] the room-temperature μ_H data for the samples of PbS-0.01Cu, $Pb_{0.99}Cu_{0.01}S$ and $Pb_{0.99}Cu_{0.01}S$-0.01Cu are noticeably higher, which caused by the reduced m^* as discussed above and comparably lower n_H in Figure 2c. Compared with the PF for p-type Na doped PbS with $SrS/CaS/ZnS/CdS$,[25,67] a noticeable enhancement of PF in Figure 6b was achieved in $Pb_{0.99}Cu_{0.01}S$-0.01Cu in the entire temperature range. As shown in Figure S20 in the Supporting Information, the thermal stability is well verified through heating and cooling cycles experiment. Figure 6c shows that simultaneously reducing κ_{tot} and enhancing PF contribute to appreciably high ZT_{ave} in $Pb_{0.99}Cu_{0.01}S$-0.01Cu. Compared with reported high-performance p-type PbS samples,[25,67] both room-temperature ZT, peak ZT and ZT_{ave} of $Pb_{0.99}Cu_{0.01}S$-0.01Cu have achieved record high values, which are ≈0.2, ≈1.2, and ≈0.79, respectively. Figure 6d displays that the PF_{ave} (300–823 K) is significantly enhanced to ≈14.9, ≈15, ≈18 μW cm⁻¹ K⁻² for PbS-0.01Cu, $Pb_{0.99}Cu_{0.01}S$, and $Pb_{0.99}Cu_{0.01}S$-0.01Cu, respectively. The PF_{ave} values obtained in this work are largely higher

than the reported Na doped PbS with $SrS/CaS/ZnS/CdS$.[25,67] Figure 6e displays the noticeable improvement on ZT_{ave} (300–823 K) of ≈0.62, ≈0.54, ≈0.79 for PbS-0.01Cu, $Pb_{0.99}Cu_{0.01}S$ and $Pb_{0.99}Cu_{0.01}S$-0.01Cu with the comparison of reported high-performance p-type PbS,[25,67] demonstrating a record-high value in this work. This high ZT_{ave} ≈ 0.79 at 300–823 K in p-type $Pb_{0.99}Cu_{0.01}S$-0.01Cu is comparable with the highest ZT_{ave} ≈ 0.72 at 300–923 K in n-type PbS,[45] which brings great potential in practical application for PbS-based thermoelectric materials. Based on the obtained ZT_{ave}, the theoretical energy conversion efficiency (η) was calculated (details can be found in Supporting Information). Compared with p-type Na doped PbS with $SrS/CaS/ZnS/CdS$ (η ≈ 8–9%),[25,67] $Pb_{0.99}Cu_{0.01}S$-0.01Cu possesses higher η of ≈13% at 300–823K due to higher average power factors (PF_{ave}).

3. Conclusions

In summary, outstanding Cu with contrasting roles could lead to high ranged performance in PbS thermoelectrics. Just adding small amount of Cu substitutions, Cu interstitials and both of them play significant roles in reducing m^* in low temperature range, and further optimizing the temperature-dependent n_H in high temperature range. The multiple positive effects of Cu contribute greatly to much enhanced PF in the entire temperature range, contributing to a record-high PF_{ave} of ≈18 μW cm⁻¹ K⁻² (300–823 K) for $Pb_{0.99}Cu_{0.01}S$-0.01Cu. Meanwhile, atomic and nanoscale semi-coherent Cu-based defects in PbS noticeably reduced κ_{lat}. Consequently, a room-temperature ZT and a peak ZT are enhanced to ≈0.2 and ≈1.2, respectively, which contributes to a record-high ZT_{ave} of ≈0.79 at 300–823 K. This work
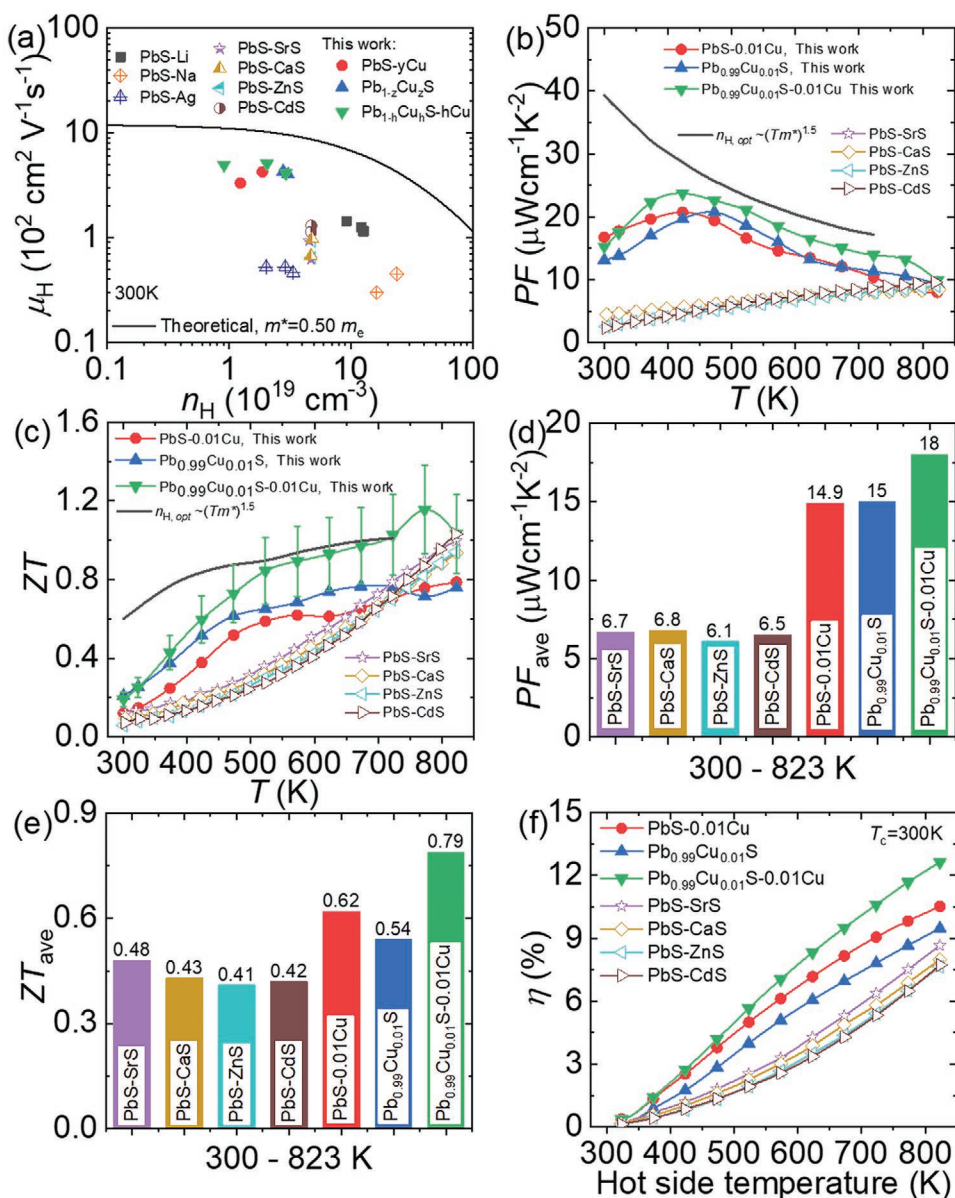
**ADVANCED
SCIENCE NEWS**

www.advancedsciencenews.com

**ADVANCED
FUNCTIONAL
MATERIALS**

www.afm-journal.de

Figure 6. Thermoelectric transport performance for p-type PbS, PbS-0.01Cu, $Pb_{0.99}Cu_{0.01}S$, and $Pb_{0.99}Cu_{0.01}S$-0.01Cu: comparison of a) μ_H, b) PF, c) ZT value, d) PF_{ave} (300–823 K), e) ZT_{ave} (300–823 K), and f) calculated efficiency. (All the samples in this work are doped with 2% Li).

indicates that synergistically optimizing n_H and m^* is of great significance for enhancing the thermoelectric performance in a wide temperature range for PbS, the present strategy could be extended to other thermoelectric systems.

4. Experimental Section

All experimental details can be found in the Supporting Information.

Supporting Information

Supporting Information is available from the Wiley Online Library or from the author.

Conflict of Interest

The authors declare no conflict of interest.

Data Availability Statement

The data that supports the findings of this study are available in the supplementary material of this article.

Keywords

[1] Y. Xiao, L.-D. Zhao, *Science* **2020**, *367*, 1196.
[2] G. Tan, L.-D. Zhao, M. G. Kanatzidis, *Chem. Rev.* **2016**, *116*, 12123.
[3] X.-L. Shi, J. Zou, Z.-G. Chen, *Chem. Rev.* **2020**, *120*, 7399.
[4] Y. Zhou, L.-D. Zhao, *Adv. Mater.* **2017**, *29*, 1702676.
[5] W. Liu, K. Yin, Q. Zhang, C. Uher, X. Tang, *Natl. Sci. Rev.* **2017**, *4*, 611.
[6] T. Zhu, Y. Liu, C. Fu, J. P. Heremans, J. G. Snyder, X. Zhao, *Adv. Mater.* **2017**, *29*, 1605884.
[7] M. Dutta, T. Ghosh, K. Biswas, *APL Mater.* **2020**, *8*, 040910.
[8] B.-C. Qin, Y. Xiao, Y.-M. Zhou, L.-D. Zhao, *Rare Met.* **2018**, *37*, 343.
[9] W.-W. Qu, X.-X. Zhang, B.-F. Yuan, L.-D. Zhao, *Rare Met.* **2018**, *37*, 79.
[10] D. Wang, Z. Huang, Y. Zhang, L. Hao, G. Wang, S. Deng, H. Wang, J. Chen, L. He, B. Xiao, Y. Xu, S. J. Pennycook, H. Wu, L.-D. Zhao, *Sci. China Mater.* **2020**, *63*, 1759.
[11] D. Wu, L.-D. Zhao, X. Tong, W. Li, L. Wu, Q. Tan, Y. Pei, L. Huang, J.-F. Li, Y. Zhu, M. G. Kanatzidis, J. He, *Energy Environ. Sci.* **2015**, *8*, 2056.
[12] Y. Pei, A. F. May, G. J. Snyder, *Adv. Energy Mater.* **2011**, *1*, 291.
[13] H. Liu, X. Yuan, P. Lu, X. Shi, F. Xu, Y. He, Y. Tang, S. Bai, W. Zhang, L. Chen, Y. Lin, L. Shi, H. Lin, X. Gao, X. Zhang, H. Chi, C. Uher, *Adv. Mater.* **2013**, *25*, 6607.
[14] T.-R. Wei, G. Tan, C.-F. Wu, C. Chang, L.-D. Zhao, J.-F. Li, G. J. Snyder, M. G. Kanatzidis, *Appl. Phys. Lett.* **2017**, *110*, 053901.
[15] S. Hui, W. Gao, X. Lu, A. Panda, T. P. Bailey, A. A. Page, S. R. Forrest, D. T. Morelli, X. Pan, K. P. Pipe, C. Uher, *Adv. Energy Mater.* **2018**, *8*, 1701623.
[16] Z.-H. Ge, D. Song, X. Chong, F. Zheng, L. Jin, X. Qian, L. Zheng, R. E. Dunin-Borkowski, P. Qin, J. Feng, *J. Am. Chem. Soc.* **2017**, *139*, 9714.
[17] J. Tang, B. Gao, S. Lin, J. Li, Z. Chen, F. Xiong, W. Li, Y. Chen, Y. Pei, *Adv. Funct. Mater.* **2018**, *28*, 1803586.
[18] B. Qin, D. Wang, W. He, Y. Zhang, H. Wu, S. J. Pennycook, L.-D. Zhao, *J. Am. Chem. Soc.* **2019**, *141*, 1141.
[19] H. Wang, Z. M. Gibbs, Y. Takagiwa, G. J. Snyder, *Energy Environ. Sci.* **2014**, *7*, 804.
[20] J. J. Kuo, S. D. Kang, K. Imasato, H. Tamaki, S. Ohno, T. Kanno, G. J. Snyder, *Energy Environ. Sci.* **2018**, *11*, 429.
[21] T. J. Slade, J. A. Grovogui, J. J. Kuo, S. Anand, T. P. Bailey, M. Wood, C. Uher, G. J. Snyder, V. P. Dravid, M. G. Kanatzidis, *Energy Environ. Sci.* **2020**, *13*, 1509.
[22] K. Lu, L. Lu, S. Suresh, *Science* **2009**, *324*, 349.
[23] D. Wu, Y. Pei, Z. Wang, H. Wu, L. Huang, L.-D. Zhao, J. He, *Adv. Funct. Mater.* **2014**, *24*, 7763.
[24] X. Qi, Y. Huang, D. Wu, B. Jiang, B. Zhu, X. Xu, J. Feng, B. Jia, Z. Shu, J. He, *J. Mater. Chem. A* **2020**, *8*, 2798.
[25] L.-D. Zhao, J. He, C.-I. Wu, T. P. Hogan, X. Zhou, C. Uher, V. P. Dravid, M. G. Kanatzidis, *J. Am. Chem. Soc.* **2012**, *134*, 7902.

[26] Y. Lan, A. J. Minnich, G. Chen, Z. Ren, *Adv. Funct. Mater.* **2010**, *20*, 357.
[27] K. Biswas, J. He, I. D. Blum, C. I. Wu, T. P. Hogan, D. N. Seidman, V. P. Dravid, M. G. Kanatzidis, *Nature* **2012**, *489*, 414.
[28] B. Cai, H.-L. Zhuang, Q. Cao, H. Hu, J. Dong, Asfandiyar, J.-F. L.i , *ACS Appl. Mater. Interfaces* **2020**, *12*, 16426.
[29] Y. Wang, W.-D. Liu, H. Gao, L.-J. Wang, M. Li, X.-L. Shi, M. Hong, H. Wang, J. Zou, Z.-G. Chen, *ACS Appl. Mater. Interfaces* **2019**, *11*, 31237.
[30] Asfandiyar, B. C. , L.-D. Zhao, J.-F. Li, *J. Materiomics* **2020**, *6*, 77.
[31] S. I. Kim, K. H. Lee, H. A. Mun, H. S. Kim, S. W. Hwang, J. W. Roh, D. J. Yang, W. H. Shin, X. S. Li, Y. H. Lee, G. J. Snyder, S. W. Kim, *Science* **2015**, *348*, 109.
[32] Y.-l. Pei, C. Chang, Z. Wang, M. Yin, M. Wu, G. Tan, H. Wu, Y. Chen, L. Zheng, S. Gong, T. Zhu, X. Zhao, L. Huang, J. He, M. G. Kanatzidis, L.-D. Zhao, *J. Am. Chem. Soc.* **2016**, *138*, 16364.
[33] Z. Chen, B. Ge, W. Li, S. Lin, J. Shen, Y. Chang, R. Hanus, G. J. Snyder, Y. Pei, *Nat. Commun.* **2017**, *8*, 13828.
[34] X. Shi, J. Yang, J. R. Salvador, M. Chi, J. Y. Cho, H. Wang, S. Bai, J. Yang, W. Zhang, L. Chen, *J. Am. Chem. Soc.* **2012**, *134*, 2842.
[35] L. You, L. Liu, X. Li, P. Nan, B. Ge, Y. Jiang, P. Luo, S. Pan, Y. Pei, W. Zhang, *Energy Environ. Sci.* **2018**, *11*, 1848.
[36] X. Qian, H. Wu, D. Wang, Y. Zhang, S. J. Pennycook, X. Gao, L. Zheng, L. D. Zhao, *Mater. Today Phys.* **2019**, *9*, 100102.
[37] W.-S. Liu, Q. Zhang, Y. Lan, S. Chen, X. Yan, Q. Zhang, H. Wang, D. Wang, G. Chen, Z. Ren, *Adv. Energy mater.* **2011**, *1*, 577.
[38] L.-D. Zhao, H. J. Wu, S. Q. Hao, C. I. Wu, X. Y. Zhou, K. Biswas, J. Q. He, T. P. Hogan, C. Uher, C. Wolverton, V. P. Dravid, M. G. Kanatzidis, *Energy Environ. Sci.* **2013**, *6*, 3346.
[39] J. Dong, J. Pei, H.-L. Zhuang, H. Hu, B. Cai, J.-F. Li, *J. Mater. Chem. A* **2019**, *7*, 27361.
[40] C. Chang, L. Zhao, *Mater. Today Phys.* **2018**, *4*, 50.
[41] X. Zhang, D. Wang, H. Wu, M. Yin, Y. Pei, S. Gong, L. Huang, S. J. Pennycook, J. He, L.-D. Zhao, *Energy Environ. Sci.* **2017**, *10*, 2420.
[42] Y. I. Ravich Yu, B. A. Efimova, I. A. Smirnov, *Semiconducting Lead Chalcogenides*, Springer, New York **1970**.
[43] Y. Xiao, D. Wang, B. Qin, J. Wang, G. Wang, L.-D. Zhao, *J. Am. Chem. Soc.* **2018**, *140*, 13097.
[44] Y. Xiao, H. Wu, J. Cui, D. Wang, L. Fu, Y. Zhang, Y. Chen, J. He, S. J. Pennycook, L.-D. Zhao, *Energy Environ. Sci.* **2018**, *11*, 2486.
[45] Y. Xiao, D. Wang, Y. Zhang, C. Chen, S. Zhang, K. Wang, G. Wang, S. J. Pennycook, G. J. Snyder, H. Wu, L.-D. Zhao, *J. Am. Chem. Soc.* **2020**, *142*, 4051.
[46] Y. Pei, Z. M. Gibbs, A. Gloskovskii, B. Balke, W. G. Zeier, G. J. Snyder, *Adv. Energy Mater.* **2014**, *4*, 1400486.
[47] Q. Zhang, Q. Song, X. Wang, J. Sun, Q. Zhu, K. Dahal, X. Lin, F. Cao, J. Zhou, S. Chen, G. Chen, J. Mao, Z. Ren, *Energy Environ. Sci.* **2018**, *11*, 933.
[48] Y. Xiao, H. Wu, D. Wang, C. Niu, Y. Pei, Y. Zhang, I. Spanopoulos, I. T. Witting, X. Li, S. J. Pennycook, G. J. Snyder, M. G. Kanatzidis, L.-D. Zhao, *Adv. Energy Mater.* **2019**, *9*, 1900414.
[49] X. Su, S. Hao, T. P. Bailey, S. Wang, I. Hadar, G. Tan, T.-B. Song, Q. Zhang, C. Uher, C. Wolverton, X. Tang, M. G. Kanatzidis, *Adv. Energy Mater.* **2018**, *8*, 1800659.
[50] Y. Xiao, H. Wu, W. Li, M. Yin, Y. Pei, Y. Zhang, L. Fu, Y. Chen, S. J. Pennycook, L. Huang, J. He, L. D. Zhao, *J. Am. Chem. Soc.* **2017**, *139*, 18732.
[51] L. You, J. Zhang, S. Pan, Y. Jiang, K. Wang, J. Yang, Y. Pei, Q. Zhu, M. T. Agne, G. J. Snyder, Z. Ren, W. Zhang, J. Luo, *Energy Environ. Sci.* **2019**, *12*, 3089.
[52] G. J. Snyder, E. S. Toberer, *Nat. Mater.* **2008**, *7*, 105.

ADVANCED
SCIENCE NEWS

www.advancedsciencenews.com

ADVANCED
FUNCTIONAL
MATERIALS

www.afm-journal.de

[53] A. F. Ioffe, L. S. Stil'bans, E. K. Iordanishvili, T. S. Stavitskaya, A. Gelbtuch, G. Vineyard, *Physics Today* **1959**, *12*, 42.

[54] H. J. Goldsmid, *Introduction to Thermoelectricity*, Vol. *121*, Springer, Berlin **2010**.

[55] Y. Xiao, L.-D. Zhao, *npj Quantum Mater.* **2018**, *3*, 55.

[56] Y.-L. Pei, Y. Liu, *J. Alloys Compd.* **2012**, *514*, 40.

[57] S. Johnsen, J. He, J. Androulakis, V. P. Dravid, I. Todorov, D. Y. Chung, M. G. Kanatzidis, *J. Am. Chem. Soc.* **2011**, *133*, 3460.

[58] L. You, J. Zhang, S. Pan, Y. Jiang, K. Wang, J. Yang, Y. Pei, Q. Zhu, M. T. Agne, G. J. Snyder, Z. Ren, W. Zhang, J. Luo, *Energy Environ. Sci.* **2019**, *12*, 3089.

[59] D. Dexter, F. Seitz, *Phys. Rev.* **1952**, *86*, 964.

[60] Y. I. Ravich, B. A. Efimova, V. I. Tamarchenko, *Phys. Status Solidi B* **1971**, *43*, 453.

[61] H. Wang, E. Schechtel, Y. Pei, G. J. Snyder, *Adv. Energy Mater.* **2013**, *3*, 488.

[62] Z. M. Gibbs, H. Kim, H. Wang, R. L. White, F. Drymiotis, M. Kaviany, G. J. Snyder, *Appl. Phys. Lett.* **2013**, *103*, 262109.

[63] Z. Chen, X. Zhang, S. Lin, L. Chen, Y. Pei, *Natl. Sci. Rev.* **2018**, *5*, 888.

[64] Z.-H. Ge, L.-D. Zhao, D. Wu, X. Liu, B.-P. Zhang, J.-F. Li, J. He, *Mater. Today* **2016**, *19*, 227.

[65] Y. Qin, Y. Xiao, L.-D. Zhao, *APL Mater.* **2020**, *8*, 010901.

[66] Y. Zheng, S. Wang, W. Liu, Z. Yin, H. Li, X. Tang, C. Uher, *J. Phys. D: Appl. Phys.* **2014**, *47*, 115303.

[67] L.-D. Zhao, J. He, S. Hao, C.-I. Wu, T. P. Hogan, C. Wolverton, V. P. Dravid, M. G. Kanatzidis, *J. Am. Chem. Soc.* **2012**, *134*, 16327.